Benchmarking calculations of wavelengths and transition rates with spectroscopic accuracy for W XLVIII through W LVI tungsten ions

Chun Yu Zhang [1], Jin Qing Li,[1] Kai Wang,[2,*] Ran Si,[1,†] Michel Godefroid [3], Per Jönsson,[4] Jun Xiao,[1]
Ming Feng Gu,[5] and Chong Yang Chen[1,‡]

[1]*Shanghai EBIT Lab, Key Laboratory of Nuclear Physics and Ion-Beam Application, Institute of Modern Physics,
Department of Nuclear Science and Technology, Fudan University, Shanghai 200433, People's Republic of China*
[2]*Hebei Key Lab of Optic-Electronic Information and Materials, The College of Physics Science and Technology,
Hebei University, Baoding 071002, People's Republic of China*
[3]*Spectroscopy, Quantum Chemistry and Atmospheric Remote Sensing (SQUARES),
CP160/09, Université Libre de Bruxelles, 1050 Brussels, Belgium*
[4]*Department of Materials Science and Applied Mathematics, Malmö University, SE-20506 Malmö, Sweden*
[5]*Space Science Laboratory, University of California, Berkeley, California 94720, USA*

Atomic properties of $n = 3$ levels for $W^{47+} - W^{55+}$ ions ($Z = 74$) are systematically calculated using two different and independent methods, namely, the second-order many-body perturbation theory and the multiconfiguration Dirac-Hartree-Fock method combined with the relativistic configuration interaction approach. Wavelengths and transition rates for electric- and magnetic-dipole transitions involving the $n = 3$ levels of $W^{47+} - W^{55+}$ are calculated. In addition, we discuss in detail the importance of the valence and core-valence electron correlations, the Breit interaction, the higher-order frequency-dependent retardation correction, and the leading quantum electrodynamical corrections for transition wavelengths. Spectroscopic accuracy is achieved for the present calculated wavelengths, and most of them agree with experimental values within 0.05%. Our calculated wavelengths, combined with collisional radiative model simulations, are used to identify the yet unidentified 25 observed lines in the extremely complex spectrum between 27 Å and 34 Å measured by Lennartsson *et al*. [Phys. Rev. A **87**, 062505 (2013)]. We provide additional data for 472 strong electric-dipole transitions in the wavelength range of 17–50 Å, and 185 strong magnetic-dipole transitions between 36 Å and 4384 Å, with a line intensity greater than 1 photon/s. These can provide benchmark data for future experiments and theoretical calculations.

I. INTRODUCTION

M-shell $W^{47+} - W^{55+}$ tungsten ions with an open $3d$ shell are of great interest in fusion research [1–5], stimulated by the proposed use of tungsten as an erosion-resistant construction material in the tokamak fusion reactors, such as ITER [6] and EAST [7,8]. The core temperature of ITER is projected to be of the order of 20 keV. At this temperature, *M*-shell tungsten ions have a large fractional abundance in the core plasmas. The x-ray and extreme ultraviolet (EUV) spectra emitted from these *M*-shell tungsten ions therefore constitute the solid base of diagnostics for ITER plasma properties such as temperature and density [4,9].

There are several measurements of $n = 3 \rightarrow 3$ wavelengths for electric-dipole (E1) and magnetic-dipole (M1) transitions of $W^{47+} - W^{55+}$ ions [10–14]. Seely *et al*. [10] identified two E1 lines of Co-like W^{47+} and Fe-like W^{48+}. Clementson and Beiersdorfer [11] measured two soft x-ray lines of E1 transitions for W^{55+} using the electron-beam ion

trap (EBIT) facility of the Lawrence Livermore National Laboratory (LLNL). Using the EBIT of the National Institute of Standards and Technology (NIST), Ralchenko *et al*. [12,13] measured one soft x-ray line of an E1 transition for W^{55+} and 41 EUV spectral lines of M1 transitions for $W^{47+} - W^{55+}$ ions. In these works [11–13], calculations using the relativistic configuration-interaction (RCI) method implemented in the flexible atomic code (FAC) [15,16] (hereafter FAC-RCI) were undertaken to identify observed lines and to provide possible identifications for most of spectral lines.

Most of the previous identifications of the $n = 3 \rightarrow 3$ E1 transitions for $W^{47+} - W^{55+}$ were due to the measurements of Lennartsson *et al*. [14] using the LLNL EBIT. As in Refs. [11–13], FAC-RCI calculations were carried out for line identification, and 17 spectral lines of E1 transitions in the wavelength range 27 Å–34 Å were successfully identified [14].

However, a significant fraction (around 60%) of the $n = 3 \rightarrow 3$ lines, i.e., 25 lines, in the soft x-ray range still awaits identification for the ions $W^{47+} - W^{55+}$. As pointed out by Lennartsson *et al*. [14], the difficulty of line identification is mainly due to insufficient electron correlations considered in their own FAC-RCI calculations. The accuracy of existing theoretical wavelengths, including those from the FAC-RCI

*wang_kai10@fudan.edu.cn
†rsi@fudan.edu.cn
‡chychen@fudan.edu.cn

calculations, did not allow firm identifications. Therefore theoretical calculations, with a precision of more than one order of magnitude better than the currently available FAC-RCI results, are urgently needed for the assignment and identification of spectral lines for the ions $W^{47+} - W^{55+}$.

To satisfy such a demand in tungsten ions with an open $3d$ shell, *ab initio* calculations were performed using the second-order relativistic many-body perturbation theory (RMBPT) [17] and the multiconfiguration Dirac-Hartree-Fock method combined with the relativistic configuration interaction (MCDHF-RCI) approach [18] for forbidden transitions within the $3s^2 3p^6 3d^q$ ($q = 1$–9) ground configurations of $W^{47+} - W^{55+}$. We should also cite other relevant theoretical calculations [1,2,19–21] that were carried out for forbidden transitions within $3s^2 3p^6 3d^q$ ($q = 1 - 9$), with a similar motivation.

By contrast, few theoretical calculations were provided for wavelengths and transition properties of E1 transitions in $W^{47+} - W^{55+}$. Using the MCDHF-RCI method implemented in the General Purpose Relativistic Atomic Structure Program (GRASP2K) package [22], Ding *et al.* [23–25] calculated wavelengths and transition rates for E1 transitions between the ground configuration $3s^2 3p^6 3d^2$ and the first excited configuration $3s^2 3p^5 3d^3$ of Ca-like W^{54+}.

The aim of this work is to provide wavelengths with spectroscopic accuracy for transitions among the $n = 3$ levels of $W^{47+} - W^{55+}$, as well as E1 and M1 transition rates. Two state-of-the-art methods, i.e., MCDHF-RCI [26] and RMBPT [27–29], are utilized. The MCDHF-RCI method was implemented in the GRASP2K code [30], which was developed by Grant [26], and improved by Froese Fischer and collaborators [30–32] in order to perform large-scale calculations. The RMBPT method was implemented in the FAC by Gu [15], using the modified multiconfigurational Dirac-Hartree-Fock-Slater (DHFS) method. It approximates the nonlocal Dirac-Hartree-Fock exchange potential by a local potential. This approximation of the electron-electron interaction potential in RMBPT is the main difference with MCDHF-RCI. The two methods have been successfully used to calculate atomic data of high accuracy in various recent studies [33–46].

The paper is organized as follows. The MCDHF-RCI and RMBPT methods are outlined in Sec. II. In Sec. III we study the relative importance of different physical effects, present our numerical results, and review the identifications of the $n = 3 \rightarrow n = 3$ transitions of $W^{47+} - W^{55+}$. In Sec. III we also try to solve the experimental identification dilemma pointed out by Lennartsson *et al.* [14] and suggest some identifications using the present MCDHF-RCI and RMBPT atomic data. The conclusions are presented in Sec. IV. If not explicitly indicated, atomic units are used throughout this work.

II. OUTLINE OF THEORY

A. MCDHF

The MCDHF-RCI method [26,31] implemented in the GRASP2K package [30] has been discussed in our recent studies [45,46]; here we only give a brief description of it. The MCDHF-RCI method starts from the Dirac-Coulomb (DC)

Hamiltonian:

$$H_{DC} = \sum_{i=1}^{N} [c\,\boldsymbol{\alpha}_i \cdot \mathbf{p}_i + V_{nuc}(r_i) + c^2(\beta_i - 1)] + \sum_{j>i=1}^{N} \frac{1}{r_{ij}},$$
(1)

where $V_{nuc}(r_i)$ is the nuclear potential, r_i is the electron-nucleus distance, r_{ij} is the distance between electrons i and j, c is the speed of light, N is the number of electrons, and $\boldsymbol{\alpha}_i$ and β_i denote the Dirac matrices.

Electron correlation is included by expressing the atomic state wave function (ASF) $\Psi(\Gamma J\pi)$ as a linear combination of configuration state functions (CSFs)

$$\Psi(\Gamma J\pi) = \sum_{i=1}^{M} c_i \Phi(\gamma_i J\pi),$$
(2)

where $\{\gamma_i\}$ specifies the occupied subshells with their complete angular coupling tree information of the CSFs, J and π are respectively the total angular momentum and the parity, and M is the number of CSFs. Each CSF, $\Phi(\gamma_i J\pi)$, is a jj-coupled many-electron function built from antisymmetrized products of one-electron Dirac orbitals [26]. The radial functions of the large and small components of the one-electron Dirac orbitals and the expansion coefficients $\{c_i\}$ of the CSFs are obtained by solving iteratively the relativistic self-consistent field (RSCF) radial equations for the orbitals, coupled to the matrix diagonalization for the targeted eigenvectors

Once the orbitals have been optimized through the MCDHF procedure, the Breit interaction and higher-order (HO) retardation correction beyond the Breit interaction, as well as the leading quantum electrodynamic (QED) effects including self-energy (SE) and vacuum polarization (VP), are added to the Dirac-Coulomb Hamiltonian in the RCI calculations to capture relativistic corrections to the Coulomb interaction (see [45,46] for more details).

It should be noted that the SE correction is evaluated with a model QED operator developed recently by Shabaev *et al.* [47,48]. It has been implemented in GRASP2K to study the ground-term fine structures of F-like [49] and Co-like ions [50] and was also used in our recent benchmark works on $W^{56+} - W^{61+}$ [45,46]. The SE correction is determined by evaluating the matrix element of the model self-energy operator,

$$h^{SE} = h_{loc}^{SE} + \sum_{i,j=1}^{n} |\phi_i\rangle \Bigg\{ \sum_{k,l=1}^{n} [(S^t)^{-1}]_{ik} \langle\psi_k| \Bigg\{ \frac{1}{2} \Big[\sum(\varepsilon_k)$$
$$+ \sum(\varepsilon_l) \Big] - h_{loc}^{SE} \Bigg\} |\psi_l\rangle (S^{-1})_{lj} \Bigg\} \langle\phi_j|,$$
(3)

with the many-electron wave function. In the latter equation, h_{loc}^{SE} is a quasilocal operator acting differently on wave functions of different angular symmetry, $\{\phi_i(\mathbf{r})\}_{i=1}^{n}$ is the model basis of projected functions, $\{\psi_i(\mathbf{r})\}_{i=1}^{n}$ is the basis of the hydrogenic wave functions, and S_{ik} is the overlap matrix element $S_{ik} = \langle\phi_i|\psi_k\rangle$. (See the original work [47,48] for more

details, including definitions of all quantities and ranges of summation.)

In the present MCDHF-RCI calculations, $\{3s^2 3p^6 3d^q$ $(q = 1 - 9)$, $3s3p^6 3d^{q+1}$ $(q = 1 - 9)$, $3s^2 3p^4 3d^{q+2}$ $(q = 1 - 8)\}$ configurations constitute the multireference (MR) spaces of even parity for $W^{47+} - W^{55+}$. Additional even configurations that differ from one ion to another complete these MR spaces: $\{3s3p^4 3d^{10}, 3p^6 3d^9\}$ for W^{49+}, $\{3p^6 3d^{10}\}$ for W^{48+}, and $\{3s^2 3p^6 3d^8 4s, 3s^2 3p^6 3d^8 4d, 3s^2 3p^5 3d^9 4p,$ $3s^2 3p^5 3d^9 4f, 3s3p^6 3d^9 4s\}$ for W^{47+}. For the odd parity, $\{3s^2 3p^5 3d^{q+1}$ $(q = 1 - 9)$, $3s^2 3p^3 3d^{q+3}$ $(q = 1 - 4, 6, 7)\}$ configurations define the MR spaces of $W^{47+} - W^{55+}$ to which the following configurations are added: $\{3s3p^5 3d^3\}$ for W^{55+}, $\{3s3p^5 3d^8\}$ for W^{50+}, $\{3s3p^5 3d^9, 3p^5 3d^{10}\}$ for W^{49+}, $\{3s3p^5 3d^{10}\}$ for W^{48+}, and $\{3s^2 3p^6 3d^8 4p, 3s^2 3p^6 3d^8 4f,$ $3s^2 3p^5 3d^9 4s, 3s^2 3p^5 3d^9 4d, 3s^2 3p^4 3d^{10} 4p\}$ for W^{47+}. For $W^{48+} - W^{55+}$, the CSF expansions are generated by allowing single (S) and double (D) excitations of the $3s$, $3p$, and $3d$ electrons, which are considered as valence (V) electrons, from all MR configurations to orbitals with $n \leqslant 7$, $l \leqslant 5$, i.e., up to h-orbital symmetry, to describe valence-valence (VV) electron correlation. The CSFs resulting from SD-MR substitutions of all $n = 2, 3$ electrons to orbitals with $n \leqslant 6$, $l \leqslant 5$, with the restriction of allowing maximum one hole in the $n = 2$ core shell, are also included in the calculations for W^{48+}–W^{55+}. These CSFs describe the core-valence (CV) electron correlation. For W^{47+}, the CSFs result from SD-MR substitutions of all the $n = 3, 4$ electrons from all MR configurations to orbitals with $n \leqslant 8$, $l \leqslant 5$. The calculations for W^{47+} differ from those performed for all the other ions because there is only one hole in the $3d$ subshell of its ground configuration $3s^2 3p^6 3d^9$, and the $3p$ and $3d$ electrons are more easily excited to the $n = 4$ shell. In other words, the $n = 3$ and $n = 4$ configurations are strongly mixed in W^{47+}. The $n = 4$ configurations are therefore included in the MR for W^{47+}, in addition to the $n = 3$ ones. The $1s$ shell is defined as an inactive closed shell in all CSFs of the expansions for the calculations of $W^{47+} - W^{55+}$. The total number of CSFs for all the $J\pi$ symmetries in the final-state expansions of W^{47+}–W^{55+} are in the range between 424 270 and 14 744 705 for even parity, and from 39 778 to 18 377 510 for odd parity. Using the concept of an active set (AS) of orbitals [33], electron correlation is included systematically, allowing the convergence to be monitored. The convergence of the present MCDHF-RCI excitation energies is achieved within 0.01%. In the present calculations, 16 processors were utilized in a parallelized version of GRASP2K.

In our previous calculations of forbidden transitions within the ground configuration $(3d^9)$ of Co-like ions with $28 \leqslant Z \leqslant 100$ [33], the CC contributions for excitation energies of W^{47+} were quantified by allowing for double excitations from each core subshell separately. It was found that the CC contribution is very small, around 0.003%. This finding is confirmed by the close agreement between our RMBPT and MCDHF-RCI results discussed in Sec. III A. The CC contribution is included in the following RMBPT but not in the MCDHF-RCI calculations for $W^{47+} - W^{55+}$. This justifies the omission of the CC electron correlation in the present MCDHF-RCI calculations.

B. RMBPT

The RMBPT method [27–29] is implemented in FAC [51,52]. This method is based on an approximation of the Dirac-Coulomb-Breit (DCB) Hamiltonian $H_{DCB} = H_{DC} + H_{Breit}$. Then the H_{DCB} operator is split into a zeroth-order model Hamiltonian H_0 and a perturbation H', i.e., $H_{DCB} = H_0 + H'$, with [27,52]

$$H_0 = \sum_i [h_d(i) + U(r_i)], \tag{4}$$

and

$$H' = -\sum_i \left[\frac{Z}{r_i} + U(r_i) \right] + \sum_{i<j} \left(\frac{1}{r_{ij}} + B_{ij} \right), \tag{5}$$

where $h_d(i)$ is the Dirac Hamiltonian for one free electron, Z is the nuclear charge, r_i is the radial coordinate of the electron i, and r_{ij} is the distance between the electrons i and j. B_{ij} is the frequency-independent Breit interaction. $U(r_i)$ is a one-electron model potential including the screening effects of all electrons, whose appropriate choice makes H' as small as possible. $U(r_i)$ is approximated by a local central potential and is derived from a Dirac-Fock-Slater self-consistent field calculation with the Hamiltonian H_0, which minimizes the weighted mean energy of all relevant configurations.

After $U(r_i)$ is determined, the eigenfunctions Φ_k^0 and eigenvalues E_k^0 of H_0 can be calculated. The Φ_k^0 is divided into a model space M and the orthogonal space N. The effect of the states outside the M space is as usual taken into account by means of a perturbation expansion and expressed in terms of an "effective" Hamiltonian H_{eff} that operates only within the M space. H_{eff} is defined as

$$H_{eff} = PH_0 P + PH'\Omega, \tag{6}$$

where P is a projection operator that produces a state Ψ_k^0 in the M space when it operates on an eigenfunction Ψ_k of the full Hamiltonian, where Ψ_k^0 is a linear combination of the subset of Φ_k^0 that belongs to the M space. Ω is the wave operator that transforms Ψ_k^0 back to Ψ_k. The eigenvalues of H_{eff} are the true eigenenergies of the full Hamiltonian.

The matrix element of the first-order H_{eff} can be written as

$$\langle \Phi(\gamma_i J\pi)|H_{eff}^{(1)}|\Phi(\gamma_j J\pi)\rangle = (H_{DCB})_{ij} + \sum_{r\in N} \frac{H'_{ir} H'_{rj}}{E_j^0 - E_r^0}, \tag{7}$$

where $(H_{DCB})_{ij} = \langle \Phi(\gamma_i J\pi)|H_{DCB}|\Phi(\gamma_j J\pi)\rangle$ and $H'_{ir} = \langle \Phi(\gamma_i J\pi)|H'|\Phi(\gamma_r J\pi)\rangle$ $(i, j \in M, r \in N)$. By solving the generalized eigenvalue problem for the first-order H_{eff}, we can obtain the eigenvalues in the second-order approximation.

The Breit interaction, the higher-order retardation correction beyond the Breit interaction, and the leading QED corrections are also considered in the same way as for the MCDHF calculations.

In the present RMBPT calculations, all possible $3s^u 3p^v 3d^w$ configurations with $k = u + v + w$ in the range between 9 and 17 are contained in the M space for $W^{47+} - W^{55+}$. Configurations that are generated from SD excitations of the M space are involved in the N space. For S and D excitations, the maximum n values are 125 and 65, respectively, and the maximum l value is 20. Besides VV and CV electron correlation, the CC electron correlation

effects are also considered in the RMBPT calculations, and SD substitutions are allowed from the $1s$ shell.

As for the GRASP2K calculations, 16 processors were utilized for the present RMBPT calculations with a parallelized version of FAC version 1.1.5 [16].

C. The collisional radiative model

To analyze the measured spectra from the EBIT experiment [14], we perform the collisional radiative model (CRM) simulations for the EBIT spectra originating from $W^{47+} -$ W^{55+}, also using the FAC version 1.1.5 [16].

In general, for a given ion, the spectral line emissivity ϵ_{ji} of a transition $j \rightarrow i$ per unit volume per unit time is written as [53]

$$\epsilon_{ji} = \frac{h\nu_{ji}}{4\pi} A_{ji} N_j, \quad (8)$$

where $h\nu_{ji}$ denotes the photon energy, A_{ji} is the spontaneous radiative transition rates from level j to i, N_j represents the population of level j per unit volume, and $1/(4\pi)$ denotes the unit solid angle.

Since the EBIT plasma electron density is low, the electron collisional excitations (ECE), de-excitations (ECD), and spontaneous radiative transition processes dominate the population mechanisms of the excited upper level j. The population of the latter, N_j, can be obtained by solving the equations under the quasi-steady-state approximation:

$$\frac{dN_j}{dt} = \sum_i N_i[n_e\alpha_{ij} + A_{ij}] - N_j \sum_i [n_e\alpha_{ji} + A_{ji}] = 0, \quad (9)$$

where n_e is the electron density, and α_{ij} and α_{ji} are, respectively, collisional populating rates and depopulating rates. $\sum_j N_j = N_Q$, where N_Q is the number density of a given W^{Q+} ion.

The equations are solved at the electron density $N_e = 5 \times 10^{12}$ cm^{-3}, the energy of electron beam $E_b = 18.2$ keV, and the energy broadening of electron beam $\Delta E_b = 30$ eV with Gaussian line distributions. These are typically parameters used in [14]. The spectra for different tungsten ions W^{Q+} are independently modeled.

Since N_Q is different in various experiments, the fractional populations per unit volume $n_j = N_j/N_Q$ are often used instead of N_j in CRM simulations, and $\sum_j n_j = 1$. Thus the intensity of an optically thin line for a given transition $j \rightarrow i$ is given by [54]

$$I_{ji} = A_{ji} n_j \quad (10)$$

in photons/s units.

In this work we present the obtained line intensity I_{ji} in Sec. III. Multiplying our I_{ji} by N_Q, the photon energy, and $1/(4\pi)$, one can derive the spectral line emissivity ϵ_{ji} for a given ion if it is needed.

In the present CRM simulations, the configurations generated by single excitations from the $n = 3$ to the $n = 4, 5$ shells are considered for $W^{55+} - W^{50+}$. Configurations having a single electron in the $n = 6$ shell are further included for $W^{49+} - W^{47+}$. ECE and ECD rates are calculated among all the included levels in the systems for $W^{47+} - W^{48+}$, while those within the $n = 3$ levels, and ECE rates from the latter

to higher-n levels are calculated for $W^{49+} - W^{55+}$. Radiative decays are considered between all the levels in the systems.

III. RESULTS AND DISCUSSION

A. Study of different physical effects

We take the Ca-like W^{54+} ion as an example of tungsten ions with an open $3d$ shell to discuss the relative importance of different physical effects on transition wavelengths, including the VV and CV electron correlations, the Breit interaction, the higher-order frequency-dependent retardation correction, and the leading QED corrections. The MCDHF-RCI and RMBPT calculations are performed to cross-check the consistency of the results.

In Table I, six $3p_{3/2} - 3d_{5/2}$ lines for E1 transitions of Ca-like W^{54+} measured by Lennartsson *et al.* [14] are listed. In this experiment, three lines (Ca-1, Ca-2, and Ca-3) were identified using the FAC-RCI calculations [14]. The other lines Ca-α, Ca-β, and Ca-γ are identified on the basis of our MCDHF-RCI and RMBPT wavelengths and CRM simulation, which is discussed in detail in Sec. III C.

When only electron correlation within the MR space is included in the MCDHF-RCI calculations, the resulting values are denoted as Dirac-Fock (DF). The DF wavelengths from our MCDHF-RCI calculations, listed in the [DF] column of Table I, are smaller than the corresponding observed values by ≈ 500 mÅ, since electron correlation is limited to the excitations within the MR spaces, i.e., $\{3s^23p^63d^2, 3s3p^63d^3, 3s^23p^43d^4\}$ and $\{3s^23p^53d^3, 3s^23p^33d^5\}$, for even and odd parity, respectively.

Furthermore, the results calculated by using the DC Hamiltonian with CSF expansions targeting electron correlations are listed in the columns labeled [DC]. For MCDHF-RCI, only VV and CV electron correlations are considered, while CC electron correlation is additionally considered for RMBPT. The addition of electron correlations brings theoretical wavelengths for these lines closer to the observations, with residual differences of the order of 200 mÅ–300 mÅ. The average difference $\pm$ the standard deviation between the RMBPT and MCDHF-RCI DC results for these six transitions are -4 mÅ $\pm$ 2 mÅ ($-0.01\% \pm 0.006\%$). This good agreement demonstrates that CC correlation, omitted in the MCDHF-RCI calculations, is indeed rather small.

The effects of VV and CV electron correlations are estimated separately through the MCDHF-RCI calculations. The VV and CV contributions to these wavelengths are found to be, respectively, 230 mÅ (0.75%) and 40 mÅ (0.1%) on average. Generally, for transitions involving valence excitations, CV electron correlation plays a smaller role than VV electron correlation. Therefore the CV electron correlation from the $2s$ and $2p$ core subshells was omitted in previous theoretical calculations [14,24]. However, considering the fact that the estimated uncertainty of experimental wavelengths provided by Lennartsson *et al.* [14] reaches a few mÅ, limiting electron correlation to VV electron correlation is not enough to reach the needed accuracy for assisting spectroscopists in the spectral lines identification process. CV effects need to be accounted for, as illustrated and discussed in our recent works [45,46].

TABLE I. Wavelengths (in Å, in vacuum) of Ca-like W^{54+} from our MCDHF-RCI and RMBPT calculations (listed in the column labeled [Final]) are compared with experimental values (Expt.) from Lennartsson *et al.* [14] and theoretical values from Ding *et al.* [24]. The estimated uncertainty of the experimental wavelength for each transition is reported in parentheses in the Expt. column. The MCDHF-RCI values calculated using the DC Hamiltonian with CSF expansions targeting only electron correlation within the MR space are listed in the column labeled [DF]. The MCDHF-RCI values calculated using the DC Hamiltonian with CSF expansions targeting VV and CV electron correlations are listed in the column labeled [DC]. The contributions (in mÅ) of different effects (VV, CV, Breit, HO, and QED) to wavelengths from our MCDHF-RCI calculations are listed in the columns labeled VV, CV, Breit, HO, and QED, respectively. The RMBPT results calculated using the DC Hamiltonian with CSF expansions targeting VV, CV, and CC electron correlations are listed in the column labeled [DC]. The contributions (in mÅ) of Breit, HO, and QED effects to wavelengths from our RMBPT calculations are also provided. The jj-coupling labels are given for each transition. The sequential numbers of energy-ordered levels are given in parentheses after the jj-coupling labels, and their detailed description can be found in the Supplemental Material [55]. Three lines (Ca-1, Ca-2, and Ca-3) were identified by Lennartsson *et al.* [14], whereas the other lines Ca-α, Ca-β, and Ca-γ are identified on the basis of our MCDHF-RCI and RMBPT results and CRM simulations (see Sec. III C for details).

	Lower state		Upper state				MCDHF-RCI								RMBPT				
Line	jj-coupling	J^π	jj-coupling	J^π	Expt.	Ding	[DF]	VV	CV	[DC]	Breit	HO	QED	[Final]	[DC]	Breit	HO	QED	[Final]
Ca-1	$3s^2 3p^6 3d_{3/2}^2(1)$	2^+	$3s^2 3p_{1/2}^2(3p_{3/2}^3 3d_{3/2}^2)_{3/2} 3d_{5/2}(34)$	3^-	31.430(1)	31.41	30.878	247	34	31.159	259	-33	47	31.433	31.154	266	-33	47	31.435
Ca-2	$3s^2 3p^6 3d_{3/2}^2(1)$	2^+	$3s^2 3p_{1/2}^2(3p_{3/2}^3 3d_{3/2}^2)_{5/2} 3d_{5/2}(33)$	2^-	31.563(2)	31.54	31.033	224	41	31.298	257	-33	48	31.570	31.291	263	-33	48	31.570
Ca-3	$3s^2 3p^6 3d_{3/2}^2(1)$	2^+	$3s^2 3p_{1/2}^2(3p_{3/2}^3 3d_{3/2}^2)_{7/2} 3d_{5/2}(31)$	1^-	31.8110(9)	31.79	31.318	207	38	31.563	236	-33	49	31.814	31.558	242	-33	49	31.815
Ca-α	$3s^2 3p^6 3d_{3/2}^2(1)$	2^+	$3s^2 3p_{1/2}^2(3p_{3/2}^3 3d_{3/2}^2)_{3/2} 3d_{5/2}(38)$	1^-	29.560(2)	29.53	29.091	230	39	29.360	194	-29	41	29.566	29.359	200	-29	42	29.572
Ca-β	$3s^2 3p^6 3d_{3/2}^2(2)$	0^+	$3s^2 3p_{1/2}^2(3p_{3/2}^3 3d_{3/2}^2)_{3/2} 3d_{5/2}(38)$	1^-	31.279(2)	31.25	30.702	246	43	30.991	283	-33	46	31.287	30.988	289	-33	47	31.291
Ca-γ	$3s^2 3p^6 3d_{3/2}^2(1)$	2^+	$3s^2 3p_{1/2}^2(3p_{3/2}^3 3d_{3/2}^2)_{3/2} 3d_{5/2}(32)$	3^-	31.749(1)	31.73	31.218	218	30	31.466	274	-34	48	31.754	31.461	281	-34	48	31.756

The contribution of the Breit interaction to these transition wavelengths in Table I is found to be about 250 mÅ (0.82%) from both the MCDHF-RCI and RMBPT calculations. The higher-order frequency-dependent correction (≈ -30 mÅ) is relatively small compared with the Breit interaction but cannot be neglected for precise calculations.

When the leading QED corrections are further included in both the present MCDHF-RCI and RMBPT calculations, the differences between theoretical and observed wavelengths are of the same order of magnitude as the experimental uncertainty. The average difference $\pm$ the standard deviation from experimental wavelengths for these six transitions are 5 mÅ $\pm$ 2 mÅ (0.02% $\pm$ 0.007%) for the MCDHF-RCI results and 8 mÅ $\pm$ 3 mÅ (0.02% $\pm$ 0.01%) for the RMBPT results. The final MCDHF-RCI and RMBPT results are in good agreement with each other, with the average difference $\pm$ the standard deviation of 2 mÅ $\pm$ 2 mÅ (0.008% $\pm$ 0.007%). However, the previous MCDHF-RCI results [24] are systematically smaller than the observed wavelengths by 20 mÅ–30 mÅ.

TABLE II. Wavelengths (λ, in Å, in vacuum), transition rates (A, in s^{-1}), line strengths (S, in atomic units, a.u.), and the accuracy categories of S values (Acc., S, see text) for $W^{47+} - W^{55+}$ from the present RMBPT and MCDHF-RCI calculations are provided for strong E1 and M1 transitions involving the $n = 3$ levels with predicted intensity (I) greater than 1 photon/s and intensity fraction (Ir) greater than 0.1%, at electron density $N_e = 5 \times 10^{12}$ cm^{-3} and electron-beam energy $E_b = 18.2$ keV modeled for an EBIT spectrum. Ir of a transition line is the ratio of its intensity to that of the strongest line in a given ion. The sequential numbers of energy-ordered levels of lower state and upper state are listed in i and j columns, respectively, and their detailed description can be found in the Supplemental Material [55]. The present table is available in its entirety in the Supplemental Material [55]. Some selected strong lines are shown here for guidance regarding its form and content.

Ion	i	j	Type	λ_{RMBPT}	$\lambda_{MCDHF-RCI}$	A_{RMBPT}	$A_{MCDHF-RCI}$	S_{RMBPT}	$S_{MCDHF-RCI}$	I	Ir	Acc.(S)
Ca-a	1	101	E1	18.631	18.631	$4.949 \times 10^{+12}$	$4.973 \times 10^{+12}$	4.739×10^{-02}	4.762×10^{-02}	144	5.15×10^{-01}	A+
Sc-a	1	139	E1	18.859	18.877	$6.070 \times 10^{+12}$	$6.086 \times 10^{+12}$	4.019×10^{-02}	4.041×10^{-02}	177	3.40×10^{-01}	A
K-a	1	64	E1	19.245	19.245	$2.941 \times 10^{+12}$	$2.960 \times 10^{+12}$	2.069×10^{-02}	2.083×10^{-02}	103	1.81×10^{-01}	A+
Ca-b	1	88	E1	19.625	19.625	$2.790 \times 10^{+12}$	$2.814 \times 10^{+12}$	5.203×10^{-02}	5.248×10^{-02}	188	6.70×10^{-01}	A+
Cr-a	3	46	E1	29.190	29.216	$7.626 \times 10^{+11}$	$7.982 \times 10^{+11}$	2.808×10^{-02}	2.947×10^{-02}	30	1.24×10^{-01}	B+
Mn-a	2	24	E1	29.237	29.232	$1.178 \times 10^{+12}$	$1.208 \times 10^{+12}$	2.909×10^{-02}	2.977×10^{-02}	29	1.25×10^{-01}	A
Cr-b	2	43	E1	29.337	29.342	$4.818 \times 10^{+11}$	$4.863 \times 10^{+11}$	4.203×10^{-02}	4.244×10^{-02}	66	2.74×10^{-01}	B+
K-b	1	17	E1	34.806	34.809	$4.826 \times 10^{+09}$	$4.909 \times 10^{+09}$	6.025×10^{-04}	6.132×10^{-04}	27	4.65×10^{-02}	A
Sc-b	1	20	E1	43.129	43.134	$7.860 \times 10^{+09}$	$7.937 \times 10^{+09}$	1.245×10^{-03}	1.258×10^{-03}	36	6.97×10^{-02}	B+
Ca-c	1	13	E1	43.561	43.560	$2.482 \times 10^{+09}$	$2.500 \times 10^{+09}$	7.089×10^{-04}	7.139×10^{-04}	34	1.22×10^{-01}	A
Ca-d	1	10	E1	45.252	45.256	$6.984 \times 10^{+09}$	$7.044 \times 10^{+09}$	1.597×10^{-03}	1.611×10^{-03}	32	1.16×10^{-01}	A+
K-c	1	5	E1	47.292	47.299	$5.490 \times 10^{+09}$	$5.522 \times 10^{+09}$	1.720×10^{-03}	1.731×10^{-03}	27	4.66×10^{-02}	A+
K-d	1	3	E1	48.603	48.615	$2.365 \times 10^{+09}$	$2.398 \times 10^{+09}$	5.361×10^{-04}	5.440×10^{-04}	19	3.30×10^{-02}	A
K-e	2	8	E1	49.768	49.785	$4.575 \times 10^{+07}$	$4.583 \times 10^{+07}$	1.670×10^{-05}	1.675×10^{-05}	7	1.15×10^{-02}	B+

TABLE III. Comparison of the present RMBPT and MCDHF-RCI E1 transition wavelengths (λ, in Å, in vacuum) with the experimental results from [10–12,60]. The lines marked with an isoelectronic identifier followed by an integer (K-1, K-2, etc.) are from [14]. The lines K-I and K-II are from [11], K-III is from [12], Fe-I and Co-I are from [10]. The corresponding previous calculations reported in these experimental works are listed in the "Prev." column. The deviations $\Delta\lambda = |\lambda_{\text{Theo.}} - \lambda_{\text{Expt.}}|$ (in mÅ) between the theoretical and experimental wavelengths are also listed in the three last columns. The number reported in parentheses, after the experimental wavelength, is the experimental uncertainty. The sequential numbers of energy-ordered levels are given in parentheses after jj-coupling labels, and their detailed description can be found in the Supplemental Material [55].

	Lower state		Upper state		λ(Å)				$\Delta\lambda$(mÅ)		
Line	jj-coupling	J^π	jj-coupling	J^π	Expt.	Prev.	RMBPT	MCDHF-RCI	Prev.	RMBPT	MCDHF-RCI
K-I	$3s^23p^63d_{3/2}(1)$	$3/2^+$	$3s^23p_{1/2}3p^4_{3/2}(3d^2_{3/2})_2(67)$	$3/2^-$	19.184(8)	19.143	19.188	19.191	41	4	7
K-II	$3s^23p^63d_{3/2}(1)$	$3/2^+$	$3s^23p_{1/2}3p^4_{3/2}(3d^2_{3/2})_2(44)$	$5/2^-$	20.552(7)	20.536	20.556	20.557	16	4	5
K-1	$3s^23p^63d_{3/2}(1)$	$3/2^+$	$3s^23p^2_{1/2}(3p^3_{3/2}3d_{3/2})_23d_{5/2}(21)$	$5/2^-$	32.403(1)	32.316	32.417	32.420	87	14	17
K-2	$3s^23p^63d_{3/2}(1)$	$3/2^+$	$3s^23p^2_{1/2}(3p^3_{3/2}3d_{3/2})_33d_{5/2}(20)$	$3/2^-$	33.040(1)	33.015	33.051	33.054	25	11	14
K-III	$3s^23p^63d_{5/2}(2)$	$5/2^+$	$3s^23p^2_{1/2}3p^3_{3/2}(3d^2_{3/2})_2(6)$	$7/2^-$	66.22(3)	65.873	66.272	66.273	347	52	53
Ca-1	$3s^23p^63d^2_{3/2}(1)$	2^+	$3s^23p_{1/2}(3p^3_{3/2}3d^2_{3/2})_{3/2}3d_{5/2}(34)$	3^-	31.430(1)	31.386	31.435	31.433	44	5	3
Ca-2	$3s^23p^63d^2_{3/2}(1)$	2^+	$3s^23p_{1/2}(3p^3_{3/2}3d^2_{3/2})_{5/2}3d_{5/2}(33)$	2^-	31.563(2)	31.505	31.570	31.570	58	7	7
Ca-3	$3s^23p^63d^2_{3/2}(1)$	2^+	$3s^23p_{1/2}(3p^3_{3/2}3d^2_{3/2})_{7/2}3d_{5/2}(31)$	1^-	31.8110(9)	31.786	31.815	31.814	25	4	3
Sc-1	$3s^23p^63d^3_{3/2}(1)$	$3/2^+$	$3s^23p^2_{1/2}(3p^3_{3/2}3d^3_{3/2})_33d_{5/2}(35)$	$3/2^-$	30.181(2)	30.051	30.195	30.190	130	14	9
Sc-2	$3s^23p^63d^3_{3/2}(1)$	$3/2^+$	$3s^23p^2_{1/2}(3p^3_{3/2}3d^3_{3/2})_33d_{5/2}(34)$	$5/2^-$	30.902(1)	30.813	30.918	30.915	89	16	13
Sc-3	$3s^23p^63d^3_{3/2}(1)$	$3/2^+$	$3s^23p^2_{1/2}(3p^3_{3/2}3d^3_{3/2})_33d_{5/2}(33)$	$1/2^-$	31.379(2)	31.365	31.385	31.385	14	6	6
Ti-1	$3s^23p^63d^4_{3/2}(1)$	0^+	$3s^23p^2_{1/2}3p^3_{3/2}3d^4_{3/2}3d_{5/2}(38)$	1^-	29.968(1)	29.860	29.982	29.982	108	14	14
V-1	$3s^23p^63d^4_{3/2}3d_{5/2}(1)$	$5/2^+$	$3s^23p^2_{1/2}3p^3_{3/2}3d^4_{3/2}(3d^2_{5/2})_4(45)$	$5/2^-$	29.124(1)	29.018	29.146	29.148	106	22	24
V-2	$3s^23p^63d^4_{3/2}3d_{5/2}(1)$	$5/2^+$	$3s^23p^2_{1/2}3p^3_{3/2}3d^4_{3/2}(3d^2_{5/2})_4(43)$	$7/2^-$	30.285(2)	30.260	30.292	30.298	25	7	13
V-3	$3s^23p^63d^4_{3/2}3d_{5/2}(1)$	$5/2^+$	$3s^23p^2_{1/2}3p^3_{3/2}3d^4_{3/2}(3d^2_{5/2})_2(41)$	$7/2^-$	31.997(1)	32.053	32.003	32.013	56	6	16
Cr-1	$3s^23p^63d^4_{3/2}3d^2_{5/2}(1)$	4^+	$3s^23p^2_{1/2}3p^3_{3/2}3d^4_{3/2}(3d^3_{5/2})_{9/2}(42)$	4^-	28.894(2)	28.796	28.897	28.915	98	3	21
Mn-1	$3s^23p^63d^4_{3/2}3d^3_{5/2}(1)$	$9/2^+$	$3s^23p^2_{1/2}3p^3_{3/2}3d^4_{3/2}(3d^4_{5/2})_4(25)$	$7/2^-$	27.5702(7)	27.428	27.582	27.574	142	12	4
Fe-1	$3s^23p^63d^4_{3/2}3d^4_{5/2}(1)$	4^+	$3s^23p^2_{1/2}3p^3_{3/2}3d^4_{3/2}3d^5_{5/2}(12)$	3^-	27.5055(9)	27.362	27.514	27.499	144	8	7
Fe-I	$3s^23p^63d^4_{3/2}3d^4_{5/2}(1)$	4^+	$3s^23p^2_{1/2}3p^3_{3/2}3d^4_{3/2}3d^5_{5/2}(12)$	3^-	27.520(15)	27.516	27.514	27.499	4	6	21
Co-I	$3s^23p^63d^4_{3/2}3d^5_{5/2}(1)$	$5/2^+$	$3s^23p^2_{1/2}3p^3_{3/2}3d^{10}(3)$	$3/2^-$	27.668(15)	27.671	27.687	27.689	3	19	21
Co-1	$3s^23p^63d^4_{3/2}3d^5_{5/2}(1)$	$5/2^+$	$3s^23p^2_{1/2}3p^3_{3/2}3d^{10}(3)$	$3/2^-$	27.6821(7)	27.574	27.687	27.689	108	5	7
Co-2	$3s^23p^63d^3_{3/2}3d^6_{5/2}(2)$	$3/2^+$	$3s^23p^2_{1/2}3p^3_{3/2}3d^{10}(3)$	$3/2^-$	32.532(3)	32.383	32.539	32.530	149	7	2

B. Results

In Table II, wavelengths (λ, in Å), transition rates (A, in s^{-1}), and line strengths (S, in atomic units (a.u.) for $W^{47+} - W^{55+}$ obtained with the present RMBPT and MCDHF-RCI calculations are provided for the strong E1 and M1 transitions involving the $n = 3$ levels. We also list the line intensity (I, in photons/s) for each transition and the ratio (Ir) of this intensity to that of the strongest transition in a given ion, which are predicted with our CRM simulations at the conditions mentioned in Sec. II C. Transition rates and line strengths are given in the Babushkin gauge. For most transitions, the A values and S values computed in the Coulomb gauge agree with those evaluated in the Babushkin gauge within 2%. The Coulomb gauge results are therefore not included in the table.

The detailed information on the upper and lower levels involved in these transitions can be found in the Supplemental Material [55], where we list the excitation energies of the 176 (158, 171, 189, 162, 190, 79, 25, 5) lowest levels for W^{55+} ($W^{54+} - W^{47+}$) together with the mixing coefficients

of the many contributing CSF identifiers that are necessary to describe 95% of the eigenvector composition. The mixing coefficients are from our RMBPT calculations. It should be noted that the CSF identifiers listed in the Supplemental Material [55] are shown as the machine-readable jj-coupling labels involving the relativistic orbitals $3s+$, $3p-$, $3p+$, $3d-$, $3d+$, which correspond to the $3s_{1/2}$, $3p_{1/2}$, $3p_{3/2}$, $3d_{3/2}$, $3d_{5/2}$ labels in the following Tables I, III, and IV, respectively. In order to better identify the experimental lines from [14], we adopt their form of CSF identifier, and only the most important CSF identifier of each level is listed in Tables I, III, and IV. The sequential numbers of energy-ordered levels can be used to easily match each level presented in Tables I, III, and IV and that in the Supplemental Material [55].

In Table II there are in total 523 strong E1 transitions originating from $W^{47+} - W^{55+}$ with a line intensity greater than 1 photon/s. All these strong transitions lie in the wavelength range from 17 Å to 50 Å. The average difference $\pm$ standard deviation between our two data sets for these 523 E1 transitions is found to be 0.005% $\pm$ 0.07% for

TABLE IV. Suggestions of assignments for the 25 unidentified lines measured by Lennartsson et al. [14] based on the present RMBPT, MCDHF-RCI, and CRM calculations. Our wavelengths (λ, in Å, in vacuum) of the candidate transitions and the corresponding line intensities (I, in photons/s) as well as the intensity ratios (Ir) at electron density $N_e = 5 \times 10^{12}$ cm⁻³ and electron-beam energy $E_b = 18.2$ keV modeled for an EBIT spectrum are listed. Ir is the ratio of intensity of a transition to that of the strongest line in a given ion. The jj-coupling labels and J^π for the upper and lower states are given. The sequential numbers of energy-ordered levels are given in parentheses after jj-coupling labels, and their detailed description can be found in the Supplemental Material [55]. All of our candidates are due to E1 transitions. The FAC-RCI results for their candidates given in Ref. [14] are also listed in the "Expt" column. The deviations (Δλ, in mÅ) between different theoretical wavelengths and the measurements are presented as well. The last column indicates that if there is only one candidate given by our calculations for each measured line, we label the candidate transition as "New"; if more than one candidate is provided, it is labeled as "sbl"; if the candidate transition reported in [14] is incorrect, it is labeled as "Inc."

		Lower state		Upper state		λ(Å)			Δλ(mÅ)					
Expt. [14]	Present	jj-coupling	J^π	jj-coupling	J^π	RMBPT	MCDHF-RCI	FAC-RCI	RMBPT	MCDHF-RCI	FAC-RCI	I	Ir	Notes
27.781(4)	Mn-α	$3s^2 3p^6 3d_{3/2}^4 3d_{5/2}^3 (2)$	$3/2^+$	$3s^2 3p_{1/2}^2 3p_{3/2}^3 3d_{3/2}^3 3d_{5/2}^4 (3d_{5/2}^4)_2 (28)$	$3/2^-$	27.785	27.778		4	−3		21	0.093	New
27.856(3)	Mn-β	$3s^2 3p^6 3d_{3/2}^3 (3d_{5/2}^4)_4 (5)$	$9/2^+$	$3s^2 3p_{1/2} (3p_{3/2}^3 3d_{3/2}^3) 3 3d_{5/2}^5 (39)$	$7/2^-$	27.842	27.834		−14	−22		6	0.028	New
28.010(3)	Cr-α	$3s^2 3p^6 3d_{3/2}^4 (3d_{5/2}^2)_2 (2)$	2^+	$3s^2 3p_{1/2}^2 3p_{3/2}^3 3d_{3/2}^3 (3d_{5/2}^3)_{5/2} (46)$	1^-	28.009	28.026		−1	16		43	0.176	New
28.067(3)	Fe-α	$3s^2 3p^6 3d_{3/2}^4 3d_{5/2}^5 (2)$	2^+	$3s^2 3p_{1/2} 3p_{3/2}^3 3d_{3/2}^3 3d_{5/2}^5 (12)$	3^-	28.069	28.055		2	−12		17	0.069	New
28.1510(9) [Cr]	Cr-β	$3s^2 3p^6 3d_{3/2}^4 (3d_{5/2}^5)_4 (1)$	4^+	$3s^2 3p_{1/2} 3p_{3/2}^3 3d_{3/2}^3 (3d_{5/2}^5)_{5/2} (44)$	3^-	28.149	28.170	28.010	−2	19	−141	205	0.842	New
28.220(2) [Mn]	Mn-γ	$3s^2 3p^6 3d_{3/2}^4 3d_{5/2}^3 (3)$	$5/2^+$	$3s^2 3p_{1/2}^2 3p_{3/2}^3 3d_{3/2}^3 (3d_{5/2}^4)_2 (28)$	$3/2^-$	28.235	28.229	28.095	15	9	−125	55	0.238	New
28.243(1) [Cr]		$3s^2 3p^6 3d_{3/2}^4 (3d_{5/2}^5)_2 (2)$	2^+	$3s^2 3p_{1/2}^2 3p_{3/2}^3 3d_{3/2}^3 (3d_{5/2}^5)_{3/2} (40)$	2^-	30.726	30.746	28.444	2483	2503	201	13	0.053	Inc
	Mn-γ	$3s^2 3p^6 3d_{3/2}^4 3d_{5/2}^3 (3)$	$5/2^+$	$3s^2 3p_{1/2}^2 3p_{3/2}^3 3d_{3/2}^3 (3d_{5/2}^4)_2 (28)$	$3/2^-$	28.235	28.229		−8	−14		55	0.238	sbl
	Mn-δ	$3s^2 3p^6 3d_{3/2}^4 3d_{5/2}^3 (2)$	$3/2^+$	$3s^2 3p_{1/2}^2 3p_{3/2}^3 3d_{3/2}^3 (3d_{5/2}^5)_0 (26)$	$3/2^-$	28.251	28.246		8	3		24	0.104	sbl
	Cr-γ	$3s^2 3p^6 3d_{3/2}^3 (3d_{5/2}^5)_{9/2} (7)$	6^+	$3s^2 3p_{1/2}^2 (3p_{3/2}^3 3d_{3/2}^3) 2 (3d_{5/2}^5)_4 (70)$	5^-	28.238	28.250		−5	7		20	0.083	sbl
28.334(2) [Fe]		$3s^2 3p^6 3d_{3/2}^4 3d_{5/2}^4 (3)$	0^+	$3s^2 3p_{1/2}^2 3p_{3/2}^3 3d_{3/2}^4 3d_{5/2}^5 (13)$	1^-	28.575	28.566	28.467	241	232	133	21	0.083	Inc
	V-α	$3s^2 3p^6 3d_{3/2}^4 (3d_{5/2}^5)_2 (5)$	$3/2^+$	$3s^2 3p_{1/2} (3p_{3/2}^3 3d_{3/2}^3) 3 (3d_{5/2}^3)_{3/2} (85)$	$3/2^-$	28.333	28.337		−1	3		1	0.003	sbl
	Ti-α	$3s^2 3p^6 3d_{3/2}^3 (3d_{5/2}^4)_4 (2)$	1^+	$3s^2 3p_{1/2} (3p_{3/2}^3 3d_{3/2}^3) 3 (3d_{5/2}^5)_4 (72)$	1^-	28.313	28.314		−21	−20		1	0.002	sbl
28.558(2) [Cr]		$3s^2 3p^6 3d_{3/2}^4 (3d_{5/2}^5)_2 (2)$	2^+	$3s^2 3p_{1/2}^2 3p_{3/2}^3 3d_{3/2}^3 (3d_{5/2}^3)_{5/2} (44)$	3^-	28.652	28.676	28.504	94	118	−54	16	0.066	Inc
	Fe-β	$3s^2 3p^6 3d_{3/2}^4 3d_{5/2}^4 (3)$	0^+	$3s^2 3p_{1/2}^2 3p_{3/2}^3 3d_{3/2}^4 3d_{5/2}^5 (13)$	1^-	28.575	28.566		17	8		21	0.083	New
28.583(2) [Mn]	Mn-ε	$3s^2 3p^6 3d_{3/2}^4 3d_{5/2}^3 (3)$	$5/2^+$	$3s^2 3p_{1/2}^2 3p_{3/2}^3 3d_{3/2}^3 (3d_{5/2}^4)_4 (27)$	$5/2^-$	28.591	28.587	28.511	8	4	−72	68	0.292	New
28.798(3)	Cr-δ	$3s^2 3p^6 3d_{3/2}^3 (3d_{5/2}^5)_4 (1)$	4^+	$3s^2 3p_{1/2}^2 3p_{3/2}^3 3d_{3/2}^3 (3d_{5/2}^5)_{5/2} (43)$	3^-	28.809	28.812		11	14		2	0.009	New
28.837(3)	Mn-ζ	$3s^2 3p^6 3d_{3/2}^4 3d_{5/2}^3 (3)$	$5/2^+$	$3s^2 3p_{1/2}^2 3p_{3/2}^3 3d_{3/2}^3 (3d_{5/2}^5)_4 (25)$	$7/2^-$	28.844	28.839		7	2		21	0.089	New
28.9910(8) [Fe]		$3s^2 3p^6 3d_{3/2}^4 3d_{5/2}^4 (2)$	2^+	$3s^2 3p_{1/2}^2 3p_{3/2}^3 3d_{3/2}^4 3d_{5/2}^5 (11)$	2^-	29.047	29.036	28.967	56	45	−24	84	0.338	Inc
	V-β	$3s^2 3p^6 3d_{3/2}^4 3d_{5/2}^3 (1)$	$5/2^+$	$3s^2 3p_{1/2}^2 3p_{3/2}^3 3d_{3/2}^3 (3d_{5/2}^4)_2 (46)$	$3/2^-$	29.007	29.005		16	14		235	0.595	New
29.0360(8) [Mn]		$3s^2 3p^6 3d_{3/2}^4 3d_{5/2}^3 (1)$	$9/2^+$	$3s^2 3p_{1/2}^2 3p_{3/2}^3 3d_{3/2}^3 (3d_{5/2}^4)_4 (23)$	$9/2^-$	29.127	29.122	29.051	91	86	15	205	0.885	Inc
[Fe]	Fe-γ	$3s^2 3p^6 3d_{3/2}^4 3d_{5/2}^4 (1)$	4^+	$3s^2 3p_{1/2}^2 3p_{3/2}^3 3d_{3/2}^4 3d_{5/2}^5 (10)$	4^-	29.043	29.033	29.044	7	−3	8	125	0.507	sbl
	Fe-δ	$3s^2 3p^6 3d_{3/2}^4 3d_{5/2}^4 (2)$	2^+	$3s^2 3p_{1/2}^2 3p_{3/2}^3 3d_{3/2}^4 3d_{5/2}^5 (11)$	2^-	29.047	29.036		11	0		84	0.338	sbl

TABLE IV. (*Continued.*)

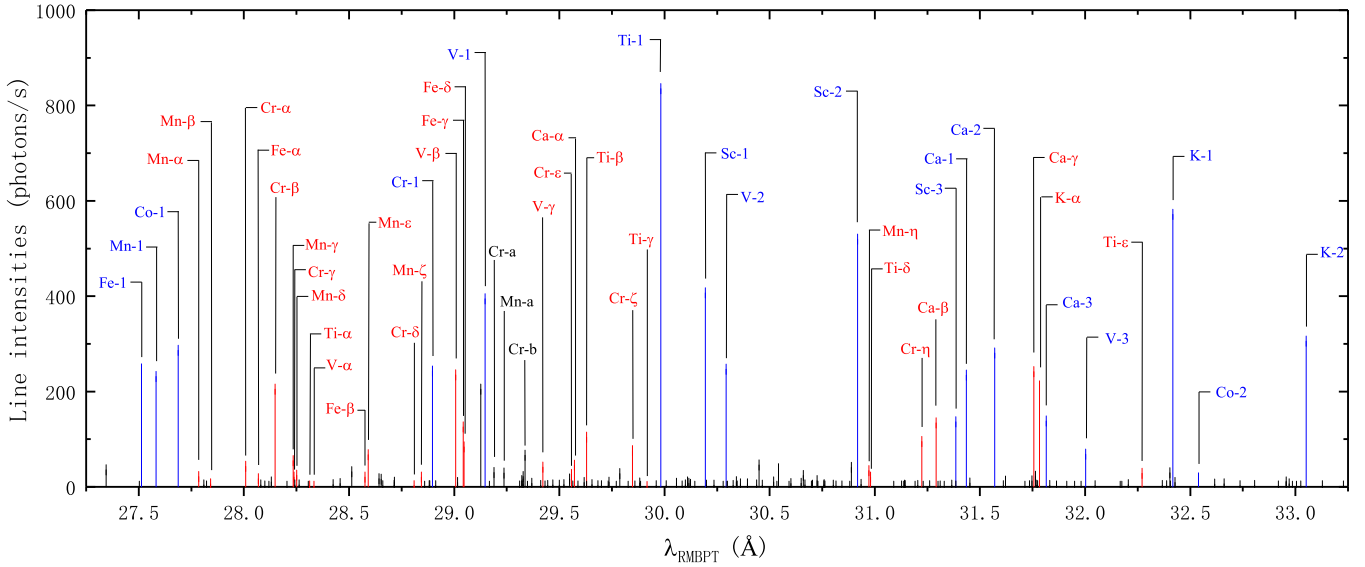| Expt. [14]	Present	Lower state jj-coupling	J^π	Upper state jj-coupling	J^π	λ(Å) RMBPT	MCDHF-RCI	FAC-RCI	$\Delta\lambda$(mÅ) RMBPT	MCDHF-RCI	FAC-RCI	I	Ir	Notes
29.399(2) [Cr]		$3s^23p^63d^4_{3/2}(3d^4_{5/2})2(2)$	2^+	$3s^23p^2_{1/2}3p^3_{3/2}3d^4_{3/2}(3d^3_{5/2})5/2(43)$	3^-	29.337	29.341	29.331	-62	-58	-68	66	0.274	Inc
[Ti]		$3s^23p^63d^3_{3/2}3d_{5/2}(5)$	3^+	$3s^23p^2_{1/2}(3p^3_{3/2}3d^3_{3/2})3(3d^3_{5/2})2(73)$	2^-	29.549	29.546	29.415	150	147	16	17	0.020	Inc
[Ca]		$3s^23p^63d^2_{3/2}(1)$	2^+	$3s^23p^2_{1/2}(3p^3_{3/2}3d^2_{3/2})3/2 3d_{5/2}(38)$	1^-	29.572	29.566	29.452	173	167	53	45	0.161	Inc
[Cr]		$3s^23p^63d^3_{3/2}(3d^3_{5/2})9/2(7)$	6^+	$3s^23p^2_{1/2}(3p^3_{3/2}3d^3_{3/2})3(3d^4_{5/2})4(62)$	6^-	29.558	29.585	29.497	159	186	98	26	0.107	Inc
[V]	V-γ	$3s^23p^63d^4_{3/2}(3d^2_{5/2})4(4)$	$11/2^+$	$3s^23p^2_{1/2}(3p^3_{3/2}3d^3_{3/2})3(3d^4_{5/2})9/2(77)$	$11/2^-$	29.421	29.426	29.301	22	27	-98	41	0.105	New
29.560(2) [Ti]		$3s^23p^63d^3_{3/2}3d_{5/2}(5)$	3^+	$3s^23p^2_{1/2}(3p^3_{3/2}3d^3_{3/2})2(3d^4_{5/2})2(70)$	3^-	29.788	29.785	29.654	228	225	94	27	0.033	Inc
[Ca]	Ca-α	$3s^23p^63d^2_{3/2}(1)$	2^+	$3s^23p^2_{1/2}(3p^3_{3/2}3d^2_{3/2})3/2 3d_{5/2}(38)$	1^-	29.572	29.566	29.452	12	6	-108	45	0.161	sbl
[Cr]	Cr-ε	$3s^23p^63d^3_{3/2}(3d^3_{5/2})9/2(7)$	6^+	$3s^23p^2_{1/2}(3p^3_{3/2}3d^3_{3/2})3(3d^4_{5/2})4(62)$	6^-	29.558	29.585	29.497	-2	25	-63	26	0.107	sbl
29.615(1) [Ti]		$3s^23p^63d^3_{3/2}3d_{5/2}(5)$	3^+	$3s^23p^2_{1/2}(3p^3_{3/2}3d^3_{3/2})2(3d^4_{5/2})2(70)$	3^-	29.788	29.785	29.654	173	170	39	27	0.033	Inc
	Ti-β	$3s^23p^63d^3_{3/2}3d_{5/2}(3)$	4^+	$3s^23p^2_{1/2}(3p^3_{3/2}3d^3_{3/2})3(3d^4_{5/2})2(69)$	4^-	29.629	29.631		14	16		104	0.125	New
29.864(3) [Cr]	Cr-ζ	$3s^23p^63d^4_{3/2}(3d^2_{5/2})2(2)$	2^+	$3s^23p^2_{1/2}3p^3_{3/2}3d^4_{3/2}(3d^4_{5/2})5/2(41)$	2^-	29.848	29.879	29.800	-16	15	-64	76	0.313	New
29.928(1)	Ti-γ	$3s^23p^6(3d^4_{3/2})2(3d^2_{5/2})4(8)$	4^+	$3s^23p^2_{1/2}[3p^3_{3/2}3d^3_{3/2}]2 17/2(3d^4_{5/2})9/2(111)$	4^-	29.917	29.923		-11	-5		1	0.001	New
30.966(2) [Ti]		$3s^23p^63d^3_{3/2}3d_{5/2}(3)$	4^+	$3s^23p^2_{1/2}(3p^3_{3/2}3d^3_{3/2})3(3d^4_{5/2})4(60)$	5^-	30.888	30.892	30.883	-78	-74	-83	41	0.049	Inc
[Mn]	Mn-η	$3s^23p^63d^4_{3/2}3d^3_{5/2}(3)$	$5/2^+$	$3s^23p^2_{1/2}3p^3_{3/2}3d^4_{3/2}(3d^4_{5/2})(22)$	$7/2^-$	30.972	30.974	31.008	6	8	42	34	0.146	sbl
[Ti]	Ti-δ	$3s^23p^63d^3_{3/2}3d^2_{5/2}(5)$	3^+	$3s^23p^2_{1/2}(3p^3_{3/2}3d^3_{3/2})3(3d^4_{5/2})4(63)$	4^-	30.980	30.981	30.932	14	15	-34	21	0.025	sbl
31.245(3) [Ca]		$3s^23p^63d^2_{3/2}(2)$	0^+	$3s^23p^2_{1/2}(3p^3_{3/2}3d^3_{3/2})3/2 3d_{5/2}(38)$	1^-	31.291	31.287	31.155	46	42	-90	134	0.479	Inc
	Cr-η	$3s^23p^63d^4_{3/2}(3d^2_{5/2})4(1)$	4^+	$3s^23p^2_{1/2}3p^3_{3/2}3d^4_{3/2}(3d^4_{5/2})9/2(36)$	5^-	31.224	31.262		-21	17		95	0.391	New
31.279(2) [Cr]		$3s^23p^63d^4_{3/2}(3d^2_{5/2})4(1)$	4^+	$3s^23p^2_{1/2}3p^3_{3/2}3d^4_{3/2}(3d^3_{5/2})9/2(36)$	5^-	31.224	31.262	31.271	-55	-17	-8	95	0.391	Inc
	Ca-β	$3s^23p^63d^2_{3/2}(2)$	0^+	$3s^23p^2_{1/2}(3p^3_{3/2}3d^2_{3/2})3/2 3d_{5/2}(38)$	1^-	31.291	31.287		12	8		134	0.479	New
31.749(1) [K]		$3s^23p^63d_{3/2}(1)$	$3/2^+$	$3s^23p^2_{1/2}(3p^3_{3/2}3d_{3/2})3 3d_{5/2}(22)$	$1/2^-$	31.783	31.783	31.669	34	34	-80	212	0.370	Inc
	Ca-γ	$3s^23p^63d^2_{3/2}(1)$	2^+	$3s^23p^2_{1/2}(3p^3_{3/2}3d^2_{3/2})3/2 3d_{5/2}(32)$	3^-	31.756	31.754		7	5		242	0.862	New
31.776(3) [Ca]		$3s^23p^63d^2_{3/2}(1)$	2^+	$3s^23p^2_{1/2}(3p^3_{3/2}3d^2_{3/2})3/2 3d_{5/2}(32)$	3^-	31.756	31.754	31.711	-20	-22	-65	242	0.862	Inc
	K-α	$3s^23p^63d_{3/2}(1)$	$3/2^+$	$3s^23p^2_{1/2}(3p^3_{3/2}3d_{3/2})3 3d_{5/2}(22)$	$1/2^-$	31.783	31.783		7	7		212	0.370	New
32.264(4) [Ca]		$3s^23p^63d^2_{3/2}(1)$	2^+	$3s^23p^2_{1/2}(3p^3_{3/2}3d^2_{3/2})3/2 3d_{5/2}(30)$	2^-	32.403	32.402	32.416	139	138	152	29	0.105	Inc
[Ti]	Ti-ε	$3s^23p^63d^2_{3/2}3d_{5/2}(3)$	4^+	$3s^23p^2_{1/2}(3p^3_{3/2}3d^3_{3/2})3(3d^2_{5/2})2(54)$	5^-	32.271	32.276	32.289	7	12	25	28	0.034	New

FIG. 1. The RMBPT transitions with a line intensity greater than 1 photon/s at electron density $N_e = 5 \times 10^{12}$ cm^{-3} and electron-beam energy $E_b = 18.2$ keV modeled for an EBIT spectrum of W^{47+} − W^{55+} in the wavelength range of 27 Å–34 Å. The lines marked with an isoelectronic identifier followed by an integer (K-1, K-2, etc.) indicate the measured and identified lines in [14]. The lines marked with an isoelectronic identifier followed by a Greek letter (K-α and K-β, etc.) represent our candidates for the 25 observed but unidentified lines in [14]. The remaining lines without identifier may also have been observed in [14] (see their Fig. 1 in detail), but no information for them was given in [14]. All the corresponding transition data can be found in Table II.

wavelengths, and 1.5% ± 2.2% for transition rates. The uncertainty estimation method proposed by Kramida [56,57] is used to classify the accuracy of the present RMBPT and MCDHF-RCI radiative transition data, according to the NIST ASD [58] terminology (AA $\leqslant$ 1%, A+ $\leqslant$ 2%, A $\leqslant$ 3%, B+ $\leqslant$ 7%, B $\leqslant$ 10%, C+ $\leqslant$ 18%, C $\leqslant$ 25%, D+ $\leqslant$ 40%, D $\leqslant$ 50%, and E > 50%). Defining the difference δS between the present RMBPT and MCDHF-RCI line strengths as $\delta S_{ji} = |\ S_{ji}^{\text{RMBPT}} - S_{ji}^{\text{MCDHF−RCI}}\ |/\max(S_{ji}^{\text{RMBPT}}, S_{ji}^{\text{MCDHF−RCI}})$, the averaged uncertainties δS_{av} for E1 transitions in various ranges of S values in each ion can be obtained. For example, the δS_{av} of W^{55+} are assessed to be 1.1% for $10^0 > S \geqslant 10^{-1}$, 1.2% for $10^{-1} > S \geqslant 10^{-2}$, 1.5% for $10^{-2} > S \geqslant 10^{-3}$, 2.0% for $10^{-3} > S \geqslant 10^{-4}$, 3.1% for $10^{-4} > S \geqslant 10^{-5}$, 4.9% for $10^{-5} > S \geqslant 10^{-6}$. (S is given in a.u. in these range specifications.) Then, $\delta \equiv \max(\delta S_{ji}, \delta S_{\text{av}})$ is accepted as the uncertainty of each particular line strength S_{ji}. For the total 523 E1 transitions originating from W^{47+} − W^{55+} listed in Table II, about 36.5% have uncertainties $\delta \leqslant$ 2% (A+), 39.2% with $\delta \leqslant$ 3% (A), 22.9% with $\delta \leqslant$ 7% (B+), 1.0% with $\delta \leqslant$ 10% (B), and only 0.4% with $\delta \leqslant$ 18% (C+) and $\leqslant$ 25% (C). It should be noted that the uncertainty of the S value of each transition is estimated by including all transitions of each ion considered, without any restriction on the line intensity values in the uncertainty estimation procedure, although only transitions with a line intensity greater than 1 photon/s are provided in Table II.

In the wavelength range of 27 Å–34 Å, line intensities of the E1 transitions are presented in Fig. 1 as a function of our RMBPT wavelengths. This wavelength interval was covered by the experiment [14], and the strongest line from each ion is located in this range, which will be discussed in Sec. III C.

Figure 2 shows line intensities of the E1 transitions as a function of our RMBPT wavelengths in the ranges of 17 Å–24 Å and 34 Å–50 Å. The lines in these two ranges have not yet been measured in any experiment, but they are strong enough to be observed. In Fig. 2 we mark some strong lines with an isoelectronic identifier (the symbol of the chemical element) followed by a letter (K-a, K-b, etc.). These lines correspond to the $3p_{3/2} − 3d_{3/2,5/2}$ transitions of K-like, Ca-like, and Sc-like W ions.

In addition, there are in total 185 strong M1 transitions originating from W^{47+} − W^{55+} with a line intensity greater than 1 photon/s according to our calculations. These lines are located in the wavelength range of 36 Å–4384 Å, and their transition data are also given in Table II. The average difference ± standard deviation between our two data sets of wavelengths and transition rates for these 185 M1 transitions are found to be 0.008% ± 0.07% and 0.60% ± 0.43%, respectively. The uncertainties of the present RMBPT and MCDHF-RCI line-strength S values of M1 transitions in each ion are also estimated as for the E1 ones. For the total 185 M1 transitions listed in Table II, about 41.1% of M1 S values have uncertainties $\delta \leqslant$ 1% (AA), 31.4% with $\delta \leqslant$ 2% (A+), 14.6% with $\delta \leqslant$ 3% (A), and 13.0% with $\delta \leqslant$ 7% (B+).

Considering RMBPT and MCDHF-RCI as two totally independent and different methods, the agreement discussed above is highly satisfying. However, if one looks closely at the distributions of differences for all ions considered, the present MCDHF-RCI transition rates are systematically larger than the RMBPT ones by 1.5% and 0.6% for E1 and M1 transition rates, respectively. This is most likely due to the different treatments of transition-matrix elements between RMBPT and MCDHF-RCI. The former adopts a perturbation approach,
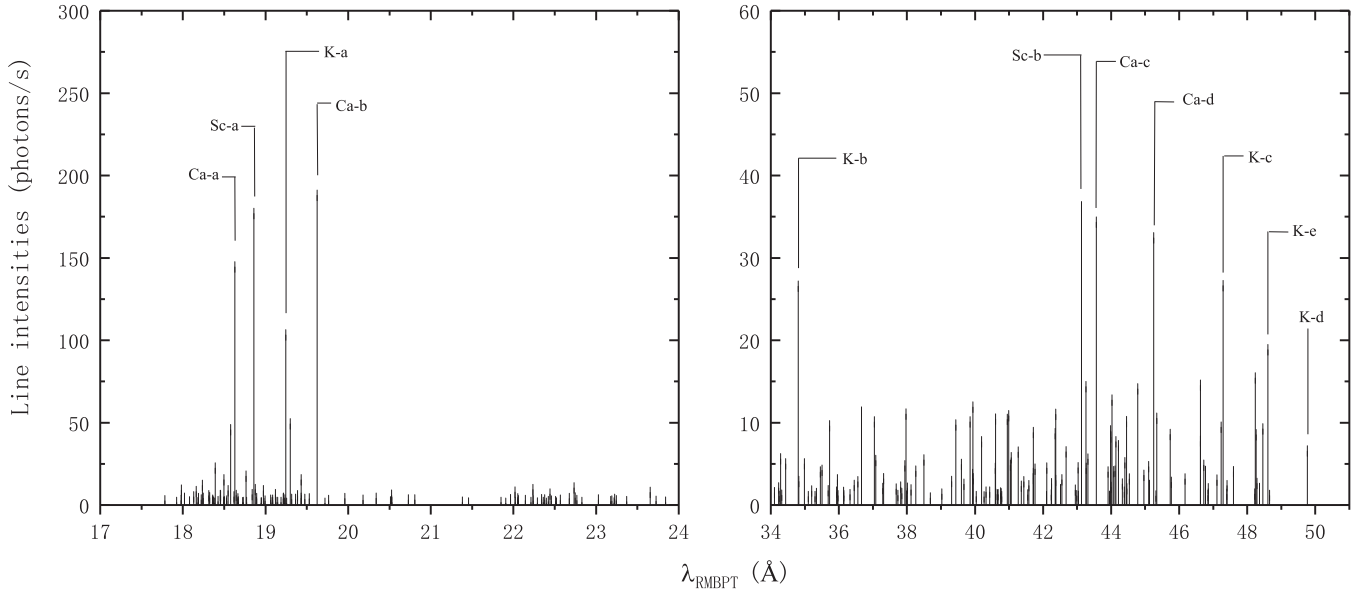
FIG. 2. The RMBPT transitions with a line intensity greater than 1 photon/s at electron density $N_e = 5 \times 10^{12}$ cm^{-3} and electron-beam energy $E_b = 18.2$ keV modeled for an EBIT spectrum of W^{47+} − W^{55+} in the wavelength ranges of 17 Å–24 Å and 34 Å– 50 Å. Some strong lines are marked with an isoelectronic identifier followed by a letter (K-a, K-b, etc.). These strong lines originate from the $3p_{3/2} - 3d_{3/2,5/2}$ transitions of K-like, Ca-like, and Sc-like W ions. All the corresponding transition information can be found in Table II.

contrary to the latter, but this argument needs further investigation. It should be mentioned that none of the MCDHF-RCI and RMBPT methods do account for the electron's anomalous magnetic moment [59]. There is no electric-quadrupole (E2) transition with a line intensity greater than 1 photon/s found in our CRM simulations for W^{47+} − W^{55+}.

C. Comparison and line identification

41 EUV spectral lines corresponding to M1 transitions between 100 Å and 250 Å from W^{47+} − W^{55+} ions were measured and identified in Ref. [13]. Using two methods, RMBPT and MCDHF-RCI, the wavelengths and transition rates within the $3s^2 3p^6 3d^q$ ($q = 1 - 9$) ground configurations were calculated for M1 transitions in our recent works [17,18]. Compared with our previous results, the present calculations are in slightly better agreement with experimental results. The average difference ± the standard deviation between the present wavelengths and experiments is found to be 72 mÅ ± 44 mÅ (0.04% ± 0.02%) for the RMBPT results and 104 mÅ ± 118 mÅ (0.06% ± 0.06%) for the MCDHF-RCI results. The improvement is mainly due to the fact that the MR configurations mentioned in Sec. II are considered in the present calculations, while only the ground configurations, i.e., $3s^2 3p^6 3d^q$ ($q = 1 - 9$), were included in the calculations of Refs. [17,18]. Hereafter we will focus on the discussion of E1 transition results.

For E1 transitions, 22 soft x-ray spectral lines in the wavelength range of 19 Å–66 Å from W^{47+} − W^{55+} ions were observed and identified in Refs. [10–12,14]. We compare the present RMBPT and MCDHF-RCI wavelengths with the measured values in Table III. The 17 spectral lines measured by Lennartsson *et al.* [14] are marked with an isoelectronic identifier (the symbol of the chemical element), followed by an integer (Al-1, Al-2, etc.). They originate from the

$3p_{3/2} - 3d_{3/2,5/2}$ transitions. The observed lines from other experiments [10–12] are marked with an isoelectronic identifier followed a Roman letter. K-I and K-II are from [11], K-III is from [12], and Fe-I and Co-I are from [10]. The corresponding FAC-RCI calculations [11,12,14] and the predicted wavelengths [60,61] helping identify the observed lines from [10] are also listed in Table III. The deviations between the different calculations and the experimental values are presented as well.

It can be seen from Table III that the present RMBPT and MCDHF-RCI calculations are in good agreement with each other, and the average difference ± standard deviations between our two data sets are found to be 5 mÅ ± 6 mÅ (0.02% ± 0.02%). The differences between the present results and measurements are within or close to the experimental uncertainties. These differences are 12 mÅ ± 11 mÅ (0.04% ± 0.02%) for the RMBPT results, and 13 mÅ ± 11 mÅ (0.04% ± 0.02%) for the MCDHF-RCI results. In addition, we can see that the present calculations show a much better agreement with experimental wavelengths [10–12,14] than the previous theoretical results. The FAC-RCI wavelengths [14] deviate from the measured values by 83 mÅ ± 76 mÅ (0.2% ± 0.2%), while the FAC-RCI results from [11,12] for K-I, K-II, and K-III lines are all smaller than the observed wavelengths by up to 347 mÅ. The predicted wavelengths of Fe-I and Co-I lines from [60,61] agree well with the measured values [10], but the good agreement is due to the interpolation or semiempirical adjustment based on the observed values. It can be seen that the present wavelengths of W^{47+} − W^{55+} are determined with a precision of more than one order of magnitude better than the previous theoretical results.

Furthermore, our accurate RMBPT and MCDHF-RCI wavelengths can assist spectroscopists in direct line identifications. Except for the 17 identified lines of W^{47+} − W^{55+} mentioned above, there are 25 unidentified spectral lines in

the experiment [14] in the wavelength range of 27 Å − 34 Å. These unidentified lines are located within four extremely complex spectral intervals, 27.70 Å − 28.70 Å, 29.20 Å − 29.80 Å, 28.80 Å − 29.20 Å, and 31.10 Å − 31.90 Å. In the first two ranges, a number of moderately intense lines were observed, but their equivalent could not be found in the theoretical modeling spectrum of Lennartsson *et al.* [14]. In the last two ranges, equally strong lines were measured with separations approximately equal to the uncertainties of their FAC-RCI calculations. Using the FAC-RCI results and CRM simulations, Lennartsson *et al.* [14] provided a few candidate transitions for some of the 25 unidentified lines, which are listed in Table IV. It is found that the deviations between the FAC-RCI results [14] and the ambiguously identified lines are 73 ± 47 mÅ (0.2% ± 0.2%). These deviations are significantly greater than the measurement uncertainties ($\leqslant 4$ mÅ). The large deviations make identification of the observed lines very difficult in the extremely complex spectra.

We also ought to mention the work of Clementson *et al.* [62], in which CRM simulations for $W^{42+} − W^{51+}$ were discussed in detail. These authors, however, focused their investigation on the x-ray transitions with $\Delta n \neq 0$ in the wavelength range of 3 Å − 12 Å at plasma conditions of relevance to magnetic fusion experiments.

In the present work we perform CRM simulations of x-ray and UV transitions with $\Delta n = 0$ for $W^{47+} − W^{55+}$. The line intensities of transitions originating from $W^{47+} − W^{55+}$ are shown as a function of our RMBPT wavelength from 27 Å to 34 Å in Fig. 1. When we compare the line features of our Fig. 1 with those of Fig. 1 from Ref. [14], there is no systematic discrepancy between the observation and our theoretical calculations. By combining the present MCDHF-RCI and RMBPT wavelengths with CRM simulations, we give our assignments and suggestions for the 25 unidentified lines from Ref. [14] in Table IV. The present candidates are marked with an isoelectronic identifier followed by a Greek letter (K-α and K-β, etc.). The deviations of the present wavelengths and the FAC-RCI results [14] from the measured values are also listed in Table IV. The corresponding line intensities of the transitions from our CRM simulations are reported as well.

It is found from Table IV that the present RMBPT and MCDHF-RCI wavelengths are in good agreement with each other, and the average difference ± standard deviation between them is found to be 9 mÅ ± 9 mÅ (0.03% ± 0.03%). The present RMBPT and MCDHF-RCI wavelengths of our candidate transitions agree well with the observed values, with the average difference ± the standard deviation of 10 mÅ ± 6 mÅ (0.03% ± 0.02%) and 11 mÅ ± 7 mÅ (0.04% ± 0.02%), respectively. Based on our calculations, there are in total 20 spectral lines identified with only one candidate for each of them, which are labeled as "New" in Table IV. More than one candidate transition is given by our calculations for each of the other five observed lines, which are considered as blended lines, labeled "sbl" in Table IV. If the candidates given in [14] are incorrect, we label them as "Inc" in Table IV. In the following we discuss the candidate transitions presented in Table IV with some examples.

The candidates provided in Ref. [14] for the four spectral lines at λ=28.1510(9) Å, 28.220(2) Å, 28.583(2) Å, and 29.864(3) Å are confirmed by the present RMBPT and

MCDHF-RCI calculations. They should be assigned to the transitions Cr-β, Mn-γ, Mn-ε, Cr-ζ, respectively. Our results are in significantly better agreement with the measurements than the previous FAC-RCI calculations [14].

There are several spectral lines for which no candidates were proposed in Ref. [14], such as the line at λ=27.781(4) Å. We give only one candidate transition $[3s^23p^2_{1/2}3p^3_{3/2}3d^4_{3/2}(3d^4_{5/2})_2]_{3/2} \rightarrow [3s^23p^63d^4_{3/2}3d^3_{5/2}]_{3/2}$ (labeled Mn-α, I=21 photons/s) for it. There is no other strong line in our simulations nearby this observed wavelength. Our RMBPT and MCDHF-RCI results for Mn-α transition are respectively 27.785 Å and 27.778 Å, and both agree with the measured value within the experimental uncertainty.

For some spectral lines, more than one candidate is given in Ref. [14], since the FAC-RCI wavelengths of these transitions depart almost "equally" from the measured values. However, some of their candidates are incorrect. For instance, the candidates for the spectral line at $\lambda = 29.0360(8)$ Å given in Ref. [14] are $[3s^23p^2_{1/2}3p^3_{3/2}3d^4_{3/2}3d^5_{5/2}]_4 \rightarrow [3s^23p^63d^4_{3/2}3d^4_{5/2}]_4$ in Fe-like W^{48+} and $[3s^23p^2_{1/2}3p^3_{3/2}3d^4_{3/2}(3d^4_{5/2})_4]_{9/2} \rightarrow [3s^23p^63d^4_{3/2}3d^3_{5/2}]_{9/2}$ in Mn-like W^{49+}. The FAC-RCI results [14] for the two transitions deviate from the measured value by 8 mÅ and 15 mÅ, respectively. Our RMBPT and MCDHF-RCI results for the former transition differ from the measured value by only 7 mÅ and −3 mÅ, respectively, but our two data sets for the latter deviate from the measurement by up to ∼90 mÅ. Additionally, the present results for the transition $[3s^23p^2_{1/2}3p^3_{3/2}3d^4_{3/2}3d^5_{5/2}]_2 \rightarrow [3s^23p^63d^4_{3/2}3d^4_{5/2}]_2$ in Fe-like W^{48+} deviate from the measured value 29.0360(8) by $\leqslant 11$ mÅ. Therefore the observed line at $\lambda = 29.0360(8)$ Å should be a blended line of the transitions $[3s^23p^2_{1/2}3p^3_{3/2}3d^4_{3/2}3d^5_{5/2}]_4 \rightarrow [3s^23p^63d^4_{3/2}3d^4_{5/2}]_4$ (labeled Fe-γ, I=125 photons/s) and $[3s^23p^2_{1/2}3p^3_{3/2}3d^4_{3/2}3d^5_{5/2}]_2 \rightarrow [3s^23p^63d^4_{3/2}3d^4_{5/2}]_2$ (labeled Fe-δ, I=84 photons/s).

For the spectral line at $\lambda = 30.966(2)$ Å, we give two candidate transitions $[3s^23p^2_{1/2}3p^3_{3/2}3d^4_{3/2}(3d^4_{5/2})_2]_{7/2} \rightarrow [3s^23p^63d^4_{3/2}3d^3_{5/2}]_{5/2}$ in Mn-like W^{49+} (labeled Mn-η, I=34 photons/s) and $[3s^23p^2_{1/2}(3p^3_{3/2}3d^3_{3/2})_3(3d^2_{5/2})_4]_4 \rightarrow [3s^23p^63d^3_{3/2}3d_{5/2}]_3$ in Ti-like W^{52+} (labeled Ti-δ, I=21 photons/s). The present RMBPT/MCDHF-RCI wavelengths are different from the measurement by 6 mÅ/8 mÅ for the Mn-η transition and by 14 mÅ/15 mÅ for the Ti-δ transition. Therefore the spectral line at $\lambda = 30.966(2)$ Å is considered as a blended line of the Mn-η and Ti-δ transitions. However, besides these two transitions, another candidate $[3s^23p^2_{1/2}(3p^3_{3/2}3d^3_{3/2})_3(3d^2_{5/2})_4]_5 \rightarrow [3s^23p^63d^3_{3/2}3d_{5/2}]_4$ in Ti-like W^{52+} was suggested by FAC-RCI calculations [14] for this spectral line, but the presently calculated wavelengths for this transition are less than the measured value by more than 70 mÅ.

It is interesting that the candidate transitions given in Ref. [14] for the spectral lines at λ=31.749(1) Å and λ=31.776(3) Å should be exchanged according to our calculations. We suggest to assign the lines at λ=31.749(1) Å to the transition $[3s^23p^2_{1/2}(3p^3_{3/2}3d^2_{3/2})_{3/2}3d_{5/2}]_3 \rightarrow [3s^23p^63d^2_{3/2}]_2$ of Ca-like W^{54+} (labeled Ca-γ, I=242 photons/s), and our RMBPT and MCDHF-RCI wavelengths for

this transition differ from the observed value by 7 mÅ and 5 mÅ, respectively. The observed line at $\lambda=31.776(1)$ Å should be assigned to the transition $[3s^2 3p_{1/2}^2(3p_{3/2}^3 3d_{3/2})_3 3d_{5/2}]_{1/2} \rightarrow [3s^2 3p^6 3d_{3/2}]_{3/2}$ of K-like W^{55+} (labeled K-α, $I=212$ photons/s), for which both corresponding wavelengths from our RMBPT and MCDHF-RCI calculations are greater than the measurement by 7 mÅ.

In addition to the E1 spectral lines discussed above, there are other 168 strong E1 transition lines with a line intensity greater than 1 photon/s found in our simulations in the wavelength range of 27 Å − 34 Å. We show them in Fig. 1, and their counterparts could be found in the experimental spectrum (Fig. 1 from Ref. [14]), such as those in the interval from about 29.19 Å to 29.34 Å. However, no measured wavelength and assignment information was given in Ref. [14]. Based on our RMBPT and MCDHF-RCI results, we provide assignments and suggestions for these lines in Table II. For example, the line at $\lambda=29.190$ Å should be assigned to the E1 transition $[3s^2 3p_{1/2}^2 3p_{3/2}^3(3d_{5/2}^3)_{5/2}]_1 \rightarrow [3s^2 3p^6 3d_{3/2}^4 3d_{5/2}^2]_0$ in Cr-like W^{50+} (labeled Cr-a, $I=30$ photons/s). The line at $\lambda=29.237$ Å should be assigned to the E1 transition $[3s^2 3p_{1/2}^2 3p_{3/2}^3 3d_{3/2}^4(3d_{5/2}^3)_2]_{1/2} \rightarrow [3s^2 3p^6 3d_{3/2}^4 3d_{5/2}^3]_{3/2}$ in Mn-like W^{49+} (labeled Mn-a, $I=29$ photons/s), and the line at $\lambda=29.337$ Å to the E1 transition $[3s^2 3p_{1/2}^2 3p_{3/2}^3 3d_{3/2}^4(3d_{5/2}^3)]_3 \rightarrow [3s^2 3p^6 3d_{3/2}^4 3d_{5/2}^2]_2$ in Cr-like W^{50+} (labeled Cr-b, $I=66$ photons/s).

IV. CONCLUSIONS

Wavelengths and E1 and M1 transition rates involving the $n=3$ levels in $W^{47+} - W^{55+}$ are calculated and cross-checked with the RMBPT and MCDHF-RCI methods. The two data sets of wavelengths and transition rates are in good agreement with each other, within 0.05% and 2%, respectively. The present calculations show a clear improvement in accuracy over previous theoretical calculations. The contributions to the transition wavelengths from VV and CV electron correlation effects, the Breit interaction, the higher-order frequency-dependent retardation correction, and the leading QED corrections are studied in detail. It is found that VV electronic correlation and Breit interaction play important roles in the calculations of transition wavelengths. Additionally, accounting for the CV electron correlation and the higher-order retardation corrections beyond the Breit interaction is important to improve the calculated wavelengths to spectroscopic accuracy.

We give suggestions of assignments for the yet unidentified 25 spectral lines measured by Lennartsson *et al.* [14] based on the present RMBPT and MCDHF-RCI calculations with spectroscopic accuracy and CRM simulations. We provide additional data for 472 strong E1 transition lines in the wavelength range of 17 Å − 50 Å and 185 strong M1 transition lines from 36 Å to 4384 Å in the Supplemental Material [55]. These strong lines are all with a line intensity greater than 1 photon/s. The information on lower and upper states of these transitions is also available in the Supplemental Material [55], where we list the excitation energies for $W^{47+} - W^{55+}$ together with the mixing coefficients of the many contributing CSF identifiers that are necessary to describe 95% of the eigenvector composition. We expect that the present complete and accurate E1 and M1 transition data for $W^{47+} - W^{55+}$ will benefit future experiments, as well as modeling and diagnosing of plasma.

[1] C. Froese Fischer, G. Gaigalas, and P. Jönsson, Atoms **5**, 7 (2017).

[2] M. S. Safronova, U. I. Safronova, S. G. Porsev, M. G. Kozlov, and Y. Ralchenko, Phys. Rev. A **97**, 012502 (2018).

[3] P. Beiersdorfer *et al.*, J. Phys. B: At. Mol. Opt. Phys. **43**, 144008 (2010).

[4] P. Beiersdorfer, J. Clementson, and U. I. Safronova, Atoms **3**, 260 (2015).

[5] J. Rzadkiewicz, Y. Yang, K. Koziol, M.G. OMullane, A. Patel, J. Xiao, K. Yao, Y. Shen, D. Lu, R. Hutton, and Y. Zou (JET Contributors), Phys. Rev. A **97**, 052501 (2018).

[6] R. J. Hawryluk, D. J. Campbell, G. Janeschitz, P. R. Thomas, R. Albanese, R. Ambrosino, C. Bachmann, L. Baylor, M. Becoulet, I. Benfatto *et al.*, Nucl. Fusion **49**, 065012 (2009).

[7] D. M. Yao, G. N. Luo, S. J. Du, L. Cao, Z. B. Zhou, T. J. Xu, X. Ji, C. L. Liu, C. Liang, Q. Li *et al.*, Fusion Eng. Des. **98-99**, 1692 (2015).

[8] L. Zhang, S. Morita, Z. W. Wu, Z. Xu, X. D. Yang, Y. X. Cheng, Q. Zang, H. Q. Liu, Y. Liu, H. M. Zhang *et al.*, Nucl. Instrum. Methods Phys. Res. Sect. A **916**, 169 (2019).

[9] J. Clementson, P. Beiersdorfer, and M. F. Gu, Phys. Rev. A **81**, 012505 (2010).

[10] J. F. Seely, C. M. Brown, and W. E. Behring, J. Opt. Soc. Am. B **6**, 3 (1989).

[11] J. Clementson and P. Beiersdorfer, Phys. Rev. A **81**, 052509 (2010).

[12] Y. Ralchenko, I. N. Draganic, J. N. Tan, J. D. Gillaspy, J. M. Pomeroy, J. Reader, U. Feldman, and G. E. Holland, J. Phys. B: At. Mol. Opt. Phys. **41**, 021003 (2008).

[13] Y. Ralchenko, I. N. Draganić, D. Osin, J. D. Gillaspy, and J. Reader, Phys. Rev. A **83**, 032517 (2011).

[14] T. Lennartsson, J. Clementson, and P. Beiersdorfer, Phys. Rev. A **87**, 062505 (2013).

[15] M. F. Gu, Can. J. Phys **86**, 675 (2008).

[16] M. F. Gu, Flexible Atomic Code, v. 1.1.5, 2017 [online], available at https://www-amdis.iaea.org/FAC/.

[17] X. L. Guo, M. Huang, J. Yan, S. Li, R. Si, C. Y. Li, C. Y. Chen, Y. S. Wang, and Y. M. Zou, J. Phys. B: At. Mol. Opt. Phys. **48**, 144020 (2015).

[18] Z. L. Zhao, K. Wang, S. Li, R. Si, C. Y. Chen, Z. B. Chen, J. Yan, and Y. Ralchenko, At. Data Nucl. Data Tables **119**, 314 (2018).

[19] P. Quinet, J. Phys. B: At. Mol. Opt. Phys. **44**, 195007 (2011).

[20] U. I. Safronova, W. R. Johnson, D. Kato, and S. Ohtani, Phys. Rev. A **63**, 032518 (2001).

[21] U. I. Safronova and A. S. Safronova, J. Phys. B: At. Mol. Opt. Phys. **43**, 074026 (2010).

[22] P. Jönsson, X. He, C. Froese Fischer, and I. P. Grant, Comput. Phys. Commun. **177**, 597 (2007).

[23] X. B. Ding, R. Sun, J. X. Liu, F. Koike, I. Murakami, D. Kato, H. A. Sakaue, N. Nakamura, and C. Z. Dong, J. Phys. B: At. Mol. Opt. Phys. **50**, 045004 (2017).

[24] X. B. Ding, R. Sun, F. Koike, I. Murakami, D. Kato, H. A. Sakaue, N. Nakamura, and C. Z. Dong, At. Data Nucl. Data Tables **119**, 354 (2018).

[25] X. Ding, J. Yang, F. Koike, I. Murakami, D. Kato, H. A. Sakaue, N. Nakamura, and C. Dong, J. Quant. Spectrosc. Radiat. Transfer **204**, 7 (2018).

[26] I. P. Grant, *Relativistic Quantum Theory of Atoms and Molecules* (Springer Science and Business Media, New York, 2007).

[27] I. Lindgren, J. Phys. B: At. Mol. Opt. Phys. **7**, 2441 (1974).

[28] M. S. Safronova, W. R. Johnson, and U. I. Safronova, Phys. Rev. A **53**, 4036 (1996).

[29] M. J. Vilkas, Y. Ishikawa, and K. Koc, Phys. Rev. A **60**, 2808 (1999).

[30] P. Jönsson, G. Gaigalas, J. Bieroń, C. Froese Fischer, and I. P. Grant, Comput. Phys. Commun. **184**, 2197 (2013).

[31] C. Froese Fischer, M. Godefroid, T. Brage, P. Jönsson, and G. Gaigalas, J. Phys. B: At. Mol. Opt. Phys. **49**, 182004 (2016).

[32] C. Froese Fischer, G. Gaigalas, P. Jönsson, and J. Bieroń, Comput. Phys. Commun. **237**, 184 (2019).

[33] X. L. Guo, R. Si, S. Li, M. Huang, R. Hutton, Y. S. Wang, C. Y. Chen, Y. M. Zou, K. Wang, J. Yan, C. Y. Li, and T. Brage, Phys. Rev. A **93**, 012513 (2016).

[34] R. Si, S. Li, X. L. Guo, Z. B. Chen, T. Brage, P. Jönsson, K. Wang, J. Yan, C. Y. Chen, and Y. M. Zou, Astrophys. J. Suppl. Ser. **227**, 16 (2016).

[35] R. Si, C. Y. Zhang, Z. Y. Cheng, K. Wang, P. Jönsson, K. Yao, M. F. Gu, and C. Y. Chen, Astrophys. J. Suppl. Ser. **239**, 3 (2018).

[36] C. Y. Zhang, R. Si, Y. W. Liu, K. Yao, K. Wang, X. L. Guo, S. Li, and C. Y. Chen, At. Data Nucl. Data Tables **121-122**, 256 (2018).

[37] C. Y. Zhang, R. Si, K. Yao, M. F. Gu, K. Wang, and C. Y. Chen, J. Quant. Spectrosc. Radiat. Transfer **206**, 180 (2018).

[38] J. Q. Li, C. Y. Zhang, R. Si, K. Wang, and C. Y. Chen, At. Data Nucl. Data Tables **126**, 158 (2019).

[39] Y. T. Li, R. Si, J. Q. Li, C. Y. Zhang, K. Yao, K. Wang, M. F. Gu, and C. Y. Chen, At. Data Nucl. Data Tables **133-134**, 101339 (2020).

[40] K. Wang, D. F. Li, H. T. Liu, X. Y. Han, B. Duan, C. Y. Li, J. G. Li, X. L. Guo, C. Y. Chen, and J. Yan, Astrophys. J. Suppl. Ser. **215**, 26 (2014).

[41] K. Wang, X. L. Guo, H. T. Liu, D. F. Li, F. Y. Long, X. Y. Han, B. Duan, J. G. Li, M. Huang, Y. S. Wang *et al.*, Astrophys. J. Suppl. Ser. **218**, 16 (2015).

[42] K. Wang, C. X. Song, P. Jönsson, G. Del Zanna, S. Schiffmann, M. Godefroid, G. Gaigalas, X. H. Zhao, R. Si, C. Y. Chen *et al.*, Astrophys. J. Suppl. Ser. **239**, 30 (2018).

[43] K. Wang, P. Jönsson, G. Gaigalas, L. Radžiūtė, P. Rynkun, G. Del Zanna, and C. Y. Chen, Astrophys. J. Suppl. Ser. **235**, 27 (2018).

[44] K. Wang, P. Jönsson, G. D. Zanna, M. Godefroid, Z. B. Chen, C. Y. Chen, and J. Yan, Astrophys. J. Suppl. Ser. **246**, 1 (2020).

[45] C. Y. Zhang, K. Wang, M. Godefroid, P. Jönsson, R. Si, and C. Y. Chen, Phys. Rev. A **101**, 032509 (2020).

[46] C. Y. Zhang, K. Wang, R. Si, M. Godefroid, P. Jönsson, J. Xiao, M. F. Gu, and C. Y. Chen, J. Quant. Spectrosc. Radiat. Transfer **269**, 107650 (2021).

[47] V. M. Shabaev, I. I. Tupitsyn, and V. A. Yerokhin, Phys. Rev. A **88**, 012513 (2013).

[48] V. M. Shabaev, I. I. Tupitsyn, and V. A. Yerokhin, Comput. Phys. Commun. **189**, 175 (2015).

[49] M. C. Li, R. Si, T. Brage, R. Hutton, and Y. M. Zou, Phys. Rev. A **98**, 020502(R) (2018).

[50] R. Si, X. L. Guo, T. Brage, C. Y. Chen, R. Hutton, and C. Froese Fischer, Phys. Rev. A **98**, 012504 (2018).

[51] M. F. Gu, At. Data Nucl. Data Tables **89**, 267 (2005).

[52] M. F. Gu, T. Holczer, E. Behar, and S. M. Kahn, Astrophys. J. **641**, 1227 (2006).

[53] A. K. Pradhan and S. N. Nahar, *Atomic Astrophysics and Spectroscopy* (Cambridge University Press, New York, 2011).

[54] E. Landi and A. Bhatia, At. Data Nucl. Data Tables **94**, 1 (2008).

[55] See Supplemental Material at http://link.aps.org/supplemental/10.1103/PhysRevA.105.022817 for level table and an expanded form of Table II.

[56] A. Kramida, Fusion Sci. Technol. **63**, 313 (2013).

[57] A. Kramida, Astrophys. J. Suppl. Ser. **212**, 11 (2014).

[58] A. Kramida, Y. Ralchenko, J. Reader, and NIST ASD Team, (2020), NIST Atomic Spectra Database (ver. 5.8), [Online]. Available at https://physics.nist.gov/asd [2021, January 21]. National Institute of Standards and Technology, Gaithersburg, MD.

[59] C. Froese Fischer, I. P. Grant, G. Gaigalas, and P. Rynkun, Phys. Rev. A **93**, 022505 (2016).

[60] J. O. Ekberg, U. Feldman, J. F. Seely, C. M. Brown, J. Reader, and N. Acquista, J. Opt. Soc. Am. B **4**, 1913 (1987).

[61] J. O. Ekberg, U. Feldman, and J. Reader, J. Opt. Soc. Am. B **5**, 1275 (1988).

[62] J. Clementson, P. Beiersdorfer, T. Brage, and M. F. Gu, At. Data Nucl. Data Tables **100**, 577 (2014).